batteries

MDPI

Article

Local Study of Lithiation and Degradation Paths in $LiMn_2O_4$ Battery Cathodes: Confocal Raman Microscopy Approach

Boris Slautin [1], Denis Alikin [1,2,*], Daniele Rosato [3], Dmitry Pelegov [1], Vladimir Shur [1] and Andrei Kholkin [1,2]

1 School of Natural Sciences and Mathematics, Ural Federal University, 620000 Ekaterinburg, Russia; boris.slautin@urfu.ru (B.S.); dmitry.pelegov@urfu.ru (D.P.), vladimir.shur@urfu.ru (V.S.); kholkin@urfu.ru or kholkin@ua.pt (A.K.)
2 Department of Physics & CICECO—Aveiro Institute of Materials, University of Aveiro, 3810–193 Aveiro, Portugal
3 Robert Bosch GmbH, 70839 Gerlingen-Schillerhoehe, Germany; daniele.rosato@seg-automotive.com
* Correspondence: denis.alikin@urfu.ru; Tel.: +343-261-74-36

Received: 26 March 2018; Accepted: 28 April 2018; Published: 1 May 2018

Abstract: Lithium manganese-based cathodes are widely used in rechargeable batteries due to their low cost, safety, and ecological stability. On the other hand, fast capacity fade occurs in $LiMn_2O_4$ mainly because of the induced manganese dissolution and formation of additional phases. Confocal Raman microscopy provides many opportunities for sensitive and spatially resolved structural studies of micro- and nanoscale phenomena. Here, we demonstrate advantages of confocal Raman spectroscopy approach for uncovering the mechanisms of lithiation/delithiation and degradation in $LiMn_2O_4$ commercial cathodes. The analysis of Raman spectra for inspecting local lithiation state and phase composition is proposed and exploited for the visualization of the inhomogeneous distribution of lithium ions. The cycling of cathodes is shown to be followed by the formation and dissolution of the Mn_3O_4 phase and local disturbance of the lithiation state. These processes are believed to be responsible for the capacity fade in the commercial batteries.

Keywords: confocal Raman microscopy; lithium manganese spinel; degradation; lithium-ion batteries

1. Introduction

The electrochemical studies of manganese oxides-based electrode materials based on $LiMn_2O_4$ (LMO) have been carried out since 1980 [1–3], thus providing an alternative to $LiCoO_2$, which had been proposed three years earlier [4]. LMO-based cathodes had been widely used in rechargeable batteries and accumulators due to their ecological stability, safety, and low cost. Wide production of lithium batteries based on LMO is motivated by the lower price of manganese and commercial availability as compared to cobalt and nickel. The advantages of the material are high discharge potential of 4 V [2] and large theoretical capacity 148 mA h g^{-1} [5].

Lithium manganese spinel has cubic *Fd3m* structure, where lithium ions occupy tetrahedral 8a sites, oxygen—32e sites. Mn^{3+} and Mn^{4+} ions are randomly distributed in the 16d crystallographic positions with 1:1 ratio of oxidization level [3,4]. During the deintercalation process, lithium ions can be extracted from LMO up to $Li_{0.015}Mn_2O_4$ phase, so-called λ-MnO_2. When completely delithiated, LMO has a very similar structure to the initial $LiMn_2O_4$, but with empty 8a lithium sites. The intermediate phase, $Li_{0.5}Mn_2O_4$, has lower symmetry (*F43m* space group) than λ-MnO_2 and $LiMn_2O_4$ [5,6].

The main problem for using LMO as a cathode material is a fade of capacity with cycling [7–11]. LMO tends to degrade during intercalation-deintercalation processes caused by the formation of poor electrochemically active structural phases and dissolution of manganese in the electrolyte on the surface of active particles [7,9,12]. The capacity loss is accelerated at elevated temperature and at high potential of the cathode, due to electrolyte instability (in fully delithiated state of λ-MnO_2) [8,9]. Cycling of LMO electrodes in a $0.6 < x < 1$ range for $Li_xMn_2O_4$ is commonly used to avoid degradation [10]. Manganese dissolution occurs due to disproportional transformation $2Mn^{3+} \rightarrow Mn^{2+} + Mn^{4+}$, when λ-$Mn^{4+}(O^{2-})_2$ oxide is formed and Mn^{2+} ions dissolve in the electrolyte [9]. Other reasons of a capacity fade in LMO are phase transformations of $LiMn_2O_4$ to $Li_2Mn_3O_7$ with MnO dissolution or to $Li_4Mn_5O_9$ with Mn_3O_4 dissolution [8]. Recently, thin Mn_3O_4 layer formation in the vicinity of active particle surface during intercalation and its further vanishing during deintercalation was demonstrated by scanning transmission electron microscopy, X-ray photoelectron spectroscopy and X-ray tomographic microscopy [7,13]. Our recent studies performed by electrochemical strain microscopy confirmed this hypothesis and quantitatively evaluated the change of local diffusion coefficient due to this undesirable phase transition during lithiation [14].

$Li_xMn_2O_4$ can be lithiated up to the $Li_2Mn_2O_4$ state, but in a range $1 < x < 2$ it has tetragonal structure and lower discharge potential of about 3 V [10]. Phase transition from cubic to tetragonal phase leads to the volume increase of 6.5%, and, therefore, fast degradation due to cracking with capacity fade occurs during cycling in this range [6,10]. "Over-lithiation" during cycling can accelerate degradation through the formation of a tetragonal phase [10]. Further studies of local variations of structural and functional material properties are crucial in order to define new strategies for reducing the electrode degradation by its modification via coating of the particles, doping or defect engineering [15–18].

Raman spectroscopy is an attractive technique for studying structural transformations in electrode materials due to its high sensitivity to small structural changes and easy-way sample preparation [6]. It was shown to be efficient for the in situ investigation of cycling processes [19–22]. Optical microscopy was also used in the past for the studying of intercalation/deintercalation of the graphite-based composites [23,24]. Harris et al. performed in situ spectral measurements for the evaluation of the state of charge (SOC) of selected oxide particles in a composite anode fabricated from a test cell and revealed that the rates at which particles deintercalate/intercalate Li ions changes with time and location [24]. The inconsistent kinetic behavior of the individual oxide particles was attributed to degradation of the electronically conducting matrix in the composite anode upon testing. In another work on meso carbon micro beads anode particles Harris et al. demonstrated diffusion anisotropy, which depends on the orientation of crystallites in the particle [23]. Migge et al. showed that intercalation in graphite particles is an inhomogeneous process, which varies with crystallographic and local conditions (temperature, electric contact etc.) [25]. Powerful combination of the Raman spectroscopy and optical microscopy, confocal Raman microscopy (CRM) approach, allows the acquisition of Raman spectra with confocal optical resolution. CRM has been applied earlier to some of the electrode materials, such as $LiNi_{0.8}Co_{0.15}Al_{0.05}O_2$ [26], $LiNi_{1/3}Co_{1/3}Mn_{1/3}O_2$ [27], $LiCoO_2$ [28], $Li_{1-x}(Ni_yCo_zAl_{1-y-z})O_2$ [29]. In $LiNi_{0.8}Co_{0.15}Al_{0.05}O_2$, $LiNi_{1/3}Co_{1/3}Mn_{1/3}O_2$, Kostecki et al. demonstrated significant non-uniformity depending on SOC within the electrode [26,27]. They used intensity of some Raman bands to visualize state of charge of the material and to evaluate its correspondence to the distribution of carbon conductive filler [26,27]. Nanda et al. also used CRM to demonstrate inhomogeneity of the SOC distribution in fresh and aged $Li_{1-x}(Ni_yCo_zAl_{1-y-z})O_2$ (NCA) cathodes and showed limitation of the ionic transport due to a decrease in the conductivity at the particle edges [29]. Nishi et al. performed CRM measurements in situ while charging/discharging the $LiCoO_2$ electrode [28]. An inhomogeneous distribution of the local state of charge in the $LiCoO_2$ electrode was observed during the 1st cycle and the distribution was broadened during the 2nd cycle. These changes in the state of charge distributions were attributed to the increase in the electronic resistance between $LiCoO_2$ particles, probably due to mechanical stress or by the formation of a solid

electrolyte interface [28]. Nowadays, new capabilities to collect and analyze big data arrays open up new perspectives to collect and store spectra by CRM with the highest possible spatial resolution (about 200–300 nm), so as to extract useful information during post-processing [30].

$LiMn_2O_4$ was intensively studied by Raman spectroscopy in the past few decades [6,31–35]. Because $LiMn_2O_4$ belong to *Fd3m* symmetry group in lithiated state it has five Raman-active modes:

$$\Gamma = A_{1g} + E_g + 3F_{2g} \quad (1)$$

The A_{1g} band near ~625 cm^{-1} relates to Mn-O bonds vibration in MnO_6 octahedra. The E_g band located at 426–432 cm^{-1} also corresponds to oxygen vibrations [5,6,31,32,35]. High-frequency scattering bands $F_{2g}(2)$ and $F_{2g}(3)$ are due to large oxygen and small manganese atom vibrations. They are localized at about ~480 cm^{-1} and ~580–590 cm^{-1}, respectively [5,6,31,32,35]. Low intensity $F_{2g}(1)$ mode near the 380 cm^{-1} is related to Li-O bond vibration [5,6,31,32,35]. Three most intensive bands at 463 cm^{-1}, 500 cm^{-1} and 590 cm^{-1} are observed for the λ-MnO_2 and connected with E_g, $F_{2g}(2)$ and A_{1g} vibration modes, correspondently [5]. In addition, one weak peak is observed at 647 cm^{-1} which is related to the $F_{2g}(3)$ vibration [5].

In the intermediate state with lower symmetry, $Li_{0.5}Mn_2O_4$, every second lithium tetragonal site is empty [36]. The vibrational modes, which are Raman inactive for $LiMn_2O_4$ and λ-MnO_2, are active for the $Li_{0.5}Mn_2O_4$. The strongest bands in the spectrum at 597 and 611 cm^{-1} correspond to the A_1 and F_2 modes (A_{1g} and $F_{2g}(3)$ modes of *Fd3m* structure) [5,31]. The weak shoulder peak near 647 cm^{-1} is usually observed and attributed to A_1 band [5,31]. Several other experimentally resolved weak peaks near 296 cm^{-1}, 493 cm^{-1}, 630 cm^{-1} are related to F_2 vibration modes [4].

Raman spectra of LMO also were studied in relation to intercalation/deintercalation processes [31,33–35]. Ab-initio calculations and experimental measurements showed the existence of high-frequency shifts of all F_{2g} modes during lithiation along with the decrease of A_{1g} frequency. $F_{1g}(1)$ peak is related to vibration of the lithium sublattice and, therefore, its intensity gradually decreases upon delithiation [31]. This mode is absent in the λ-MnO_2 state [31]. Kanoh et al. analyzed in-situ Raman spectra of thin layered LMO electrode and correlated the ratio of ~600 cm^{-1} A_{1g} mode intensities in lithiated and completely delithated state to the state of charge of the material [34]. λ-MnO_2 delithiated phase was shown to exhibit a strong enhancement of the Raman spectra intensity for the excitation wavelengths 600–640 cm^{-1} [33,34,37]. This effect was attributed to the reduction of conductivity during deintercatlation [33,34,37]. In spite of a variety of different Raman spectroscopy measurements, the strict criteria for determination of LMO material 'state of charge' are still missing.

In this contribution, we are trying to shed further light on the understanding of delithiation and degradation paths by local CRM measurements of LMO cathode material with different 'state of charge' and 'state of health' parameters. We demonstrated a possibility to qualitatively separate lithiated and delithiated states of active ionic particles. Local scale measurements performed on 'fresh' and 'aged' battery cathodes revealed significant differences in charge distribution inside distinct active particles. The particles were lithiated inhomogeneously due to the peculiarity of delithiation kinetics in the LMO cathodes. Analysis of the Raman spectra allowed to detect the appearance of Mn_3O_4 phase diluting during further cycling. Cluster analysis performed on CRM images clearly separates different lithiation states and additional phases in cathodes. The proposed approach of spatially resolved Raman spectroscopy was shown to be an attractive method for studying lithiation/delithiation processes and degradation of electrode material.

2. Materials and Methods

2.1. Sample Preparation

Samples of LMO cathodes were prepared and tested in the electrochemical cylindrical cells at Robert Bosch GmbH. $LiMn_2O_4$ cathodes were cycled against the graphite anodes at 1 C-rate from 2.5 V to 4.2 V. Cathodes with different state of charge (SOC) and state of health (SOH) were extracted from

the commercial cells (Table 1). The 'fresh' cathodes cycled 3 times at 1 C charge rate and 1 C discharge rate are referred further as 100% SOH. The 'aged' cathodes were cycled (106 times) down to 80% SOH at 1 C charge rate and 16 C discharge rate, then cycled 3 times at 1 C-rate and discharged at 1 C-rate before opening. The cells were opened in an argon-filled glove box. The cathode, separator and anode were uncoiled and separated from each other. Pieces of the cathode on the current collector were cut and washed in a dimethyl carbonate solution in order to remove the electrolyte. After that, samples were taken out of the glove box and dried. The sample sections were embedded in a commercial epoxy resin and then polished step-by-step, first, mechanically by diamond abrasive and silica suspension, and, second, by Ar ion beam milling. A more detailed procedure of sample preparation can found elsewhere [38,39].

Table 1. Electrochemical state of studied $LiMn_2O_4$ cathodes.

№ of Sample	State of Health	State of Charge	Composition	Lattice Parameter, Å
S1	100%	0%	$Li_{0.94}Mn_2O_4$	8.18
S2	100%	100%	$Li_{0.61}Mn_2O_4$	8.09
S3	80%	0%	$Li_{0.89}Mn_2O_4$	8.18
S4	80%	100%	$Li_{0.65}Mn_2O_4$	8.11

2.2. Confocal Raman Microscopy

Raman measurements were carried out using a commercial confocal Raman microscope (Alpha 300 AR, WiTec GmbH, Ulm, Germany) based on the Olympus optical setup. A 488 nm laser light was focused on the individual particle by a 100×, 0.75 NA objective which provided about 260 nm spatial resolution. Spectral measurements were done at 1800 grids per mm grating with a 1.22 cm^{-1} spectral resolution. 60 s exposure time and 5 averaging steps were used for the integral spectrum measurements. Deconvolution of the bands was done using a Peak Fit 4.0 software. The superposition of Lorenz functions was chosen for the fitting. Strong narrow peaks in the spectra, so-called 'cosmic particles', were removed using FFT filtering. The background from the CCD matrix and steady-state luminescence were also removed. All spectra were normalized by the area.

Microscopic measurements were realized by the scanning of the sample with the help of piezoelectrically driven stage. Accumulation time in each point during scanning was 25 s. In each point of the scan, full spectrum was saved as 3D-dimensional array (XY-coordinate and Raman shift) and further fitted by superposition of Lorenz functions via a home-made program written with Wolfram Mathematica package. The peak position, its amplitude and half-width were extracted and represented as pseudo-color images, where XY coordinate refers to a spatial position at the surface and color corresponds to one of the studied parameters. Gwyddion software (Department of Nanometrology, Czech Metrology Institute) was used for data treatment and final representation.

3. Results and Discussion

3.1. Integral Raman Spectroscopy Measurements

Cross-section of lithium-ion battery cathode is represented in Figure 1a in which active LMO particles embedded into polymeric matrix of polyvinylidene fluoride and carbon black are shown. This mixture was spread over both sides of a metal sheet, on which a current collector made of Al is clearly seen. The average radius of active LMO particle ranged from 5 to 10 μm. First, we compared Raman spectra integrated over the particle surface for the 'fresh' (100% SOH) and 'aged' (80% SOH) LMO cathodes in lithiated (discharged) and delithiated (charged) state (Figure 1b).

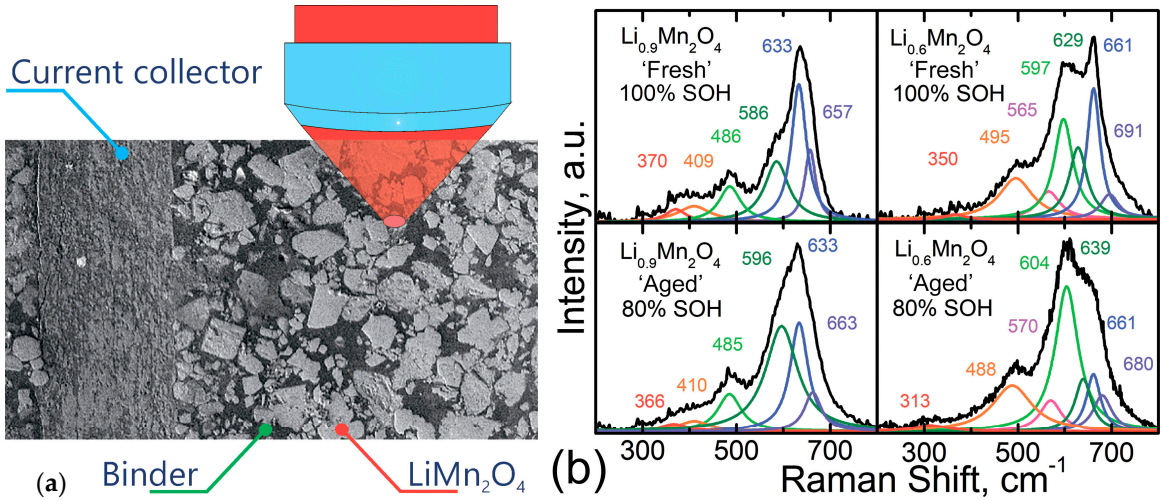

Figure 1. (**a**) Experimental scheme of the CRM measurements in $LiMn_2O_4$ (LMO) cathodes; (**b**) Raman spectra of LMO cathodes with different SOC and SOH integrated over the surface of an active particle.

The integral Raman spectra of the particles with different SOC and SOH were predictably different. We separated 6 scattering peaks in the spectra for lithiated cathodes. Major band at the 633 cm^{-1} was seen on all samples and corresponded to A_{1g} vibration. The band near the 410 cm^{-1} is associated with E_g vibration. The bands at 366–370 cm^{-1}, 485–486 cm^{-1} and 586–596 were assigned to the F_{2g} vibrations. While Raman spectra look similar in fresh and partially aged cathodes, some differences can be nevertheless found. The intensity of scattering peak at 586 cm^{-1} in aged cathodes increases and its' position shifts about 10 cm^{-1} to higher frequency.

Raman spectra of delithiated cathodes were fitted by 7 bands. Bands around of 313, 488–495, 629–639 cm^{-1} were related to F_2 vibrations. We observed also two bands related to A_1 modes between 565–570 and 597–604 cm^{-1}. Earlier Amanieu et al. also compared Raman spectra for completely lithiated and delithiated particles of LMO cathodes [40]. They related strong peak at 592 cm^{-1} for the delithiated samples to the A_{1g} vibration of the λ-MnO_2 phase [40]. However, other peaks, which are specific for the λ-MnO_2 phase were not found [6]. Thus we attributed the peak around 592 cm^{-1} to $LiMn_2O_4$ phase [6]. The weak peak near 350 cm^{-1} was found, which could not be referred to any vibration mode. Probably it is a part of a wide low-intensity luminescence plateau.

The parameters of deconvoluted Raman peaks and their assignment to different vibration bands are summarized in Table 2. It should be noted that deconvolution and evaluation of Raman shifts were difficult to do for the peaks with small intensities: E_g, $F_{2g}(1)$, $F_{2g}(2)$. That is why we focused mostly on the bands with high intensity: $F_{2g}(3)$, A_{1g}, where Raman shift can be determined more accurately. The Raman bands at about 660 cm^{-1} were observed in all samples, and they were especially strong they in delithiated LMO. We suppose that these peaks are due to the appearance of Mn_3O_4 phase during intercalation/deintercalation process [31]. The alternative explanation for delithiated state would be A_1 vibration, however the intensity of this peak must be significantly lower [6]. Besides that, the peak with the similar shift was observed in the lithiated state as well. For the delithiated samples we also observed Raman band around of 680–690 cm^{-1}, which cannot be related to LMO vibration modes. Following Ammundsen et al. [19] we linked this scattering peak to the appearance of Mn_2O_3 phase [31]. Determination of vibration mode related to this band is complicated due to its small intensity.

Table 2. Raman bands observed in spectra from LMO cathodes and correspondent vibrational modes.

$Li_{0.9}Mn_2O_4$	Fresh	Aged	$Li_{0.6}Mn_2O_4$	Fresh	Aged
$F_{2g}(1)$	370 cm^{-1}	366 cm^{-1}	F_2	350 cm^{-1}	313 cm^{-1}
E_g	409 cm^{-1}	410 cm^{-1}	F_2	495 cm^{-1}	488 cm^{-1}
$F_{2g}(2)$	486 cm^{-1}	485 cm^{-1}	A_1	565 cm^{-1}	570 cm^{-1}
$F_{2g}(3)$	586 cm^{-1}	596 cm^{-1}	A_1	597 cm^{-1}	604 cm^{-1}
A_{1g}	629 cm^{-1}	633 cm^{-1}	F_2	629 cm^{-1}	639 cm^{-1}
$A_{1g}(Mn_3O_4)$	657 cm^{-1}	663 cm^{-1}	$A_{1g}(Mn_3O_4)$	661 cm^{-1}	661 cm^{-1}
			$\nu(Mn_2O_3)$	691 cm^{-1}	680 cm^{-1}

3.2. Characterization of Lithiated State

Firstly, we analyzed the Raman band positions in completely lithiated $Li_{0.9}Mn_2O_4$ particles from fresh and aged cathodes. The maps of the $F_{2g}(3)$ and A_{1g} Raman band position are plotted in Figure 2. It is seen that the positions of the peaks change significantly (by more than 10 cm^{-1}) in some particle regions. We clearly observed the shift of F_{2g} band to higher frequency in the middle of the particles both in fresh and aged cathode, while at the edges of the particle F_{2g} band the shift was smaller (Figure 2a,c). In contrast to F_{2g} band, A_{1g} band position was lower in the middle of the particle (Figure 2b,d). These peaks clearly demonstrate an opposite behavior. Lithium intercalation/deintercalation induces the change of the atomic bond length, responsible for the corresponding bond force constant changes. This transformation directly affected the Raman bands: all F_{2g} modes shift to higher frequency and A_{1g} modes shift to the lower one [32]. Spatially resolved imaging of these shifts reveals an inhomogeneity of the lithiated phase in the middle of the particles, producing a core structure, while shell is enriched by lithium (Figure 2). This observation is in line with recent electrochemical strain microscopy measurements in the same material [14].

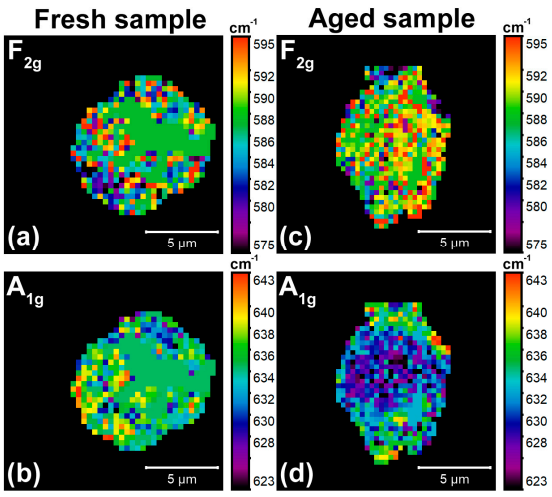

Figure 2. Mapping of the (**a**,**c**) F_{2g}, and (**b**,**d**) A_{1g} peak positions in the active ionic particles of (**a**,**b**) fresh and (**c**,**d**) aged LMO cathodes. Completely lithiated state: $Li_{0.9}Mn_2O_4$ (0% SOC).

Though Raman band position can be used as a signature of the lithiation state, the accuracy of this approach is not very high due to the apparent difficulties in the precise evaluation of the peak positions in complex Raman spectra with many overlapped peaks. Therefore, we further evaluated the 'intensity-based' parameters. Accuracy of the intensity determination is obviously better. We used two parameters for our analysis. Following the work Kanoh et al. [34] we plotted the ratio of A_{1g} and F_{2g} peak intensities, which was shown to be influenced by the material state of charge. Decrease of this ratio in the border of the particles was related to its' preferable lithiation. Maps of this ratio

(Figure 3a,c) correlate to those constructed by the peak position. We refer thereby the ratio of A_{1g} and F_{2g} peak intensities to be roughly proportional to the "state of charge".

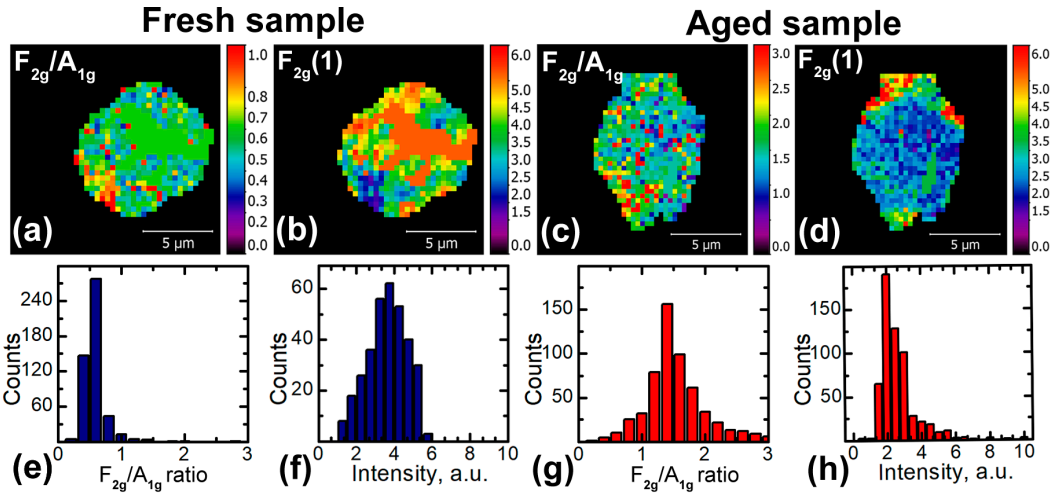

Figure 3. Mapping of the (**a**,**c**) ratio between F_{2g}/A_{1g} peak intensities (**b**,**d**) $F_{2g}(1)$ peak intensity in the active ionic particles of (**a**,**b**) fresh and (**c**,**d**) aged LMO cathodes; (**e**–**h**) histograms of the signal corresponding to maps (**a**–**d**). Completely lithiated state: $Li_{0.9}Mn_2O_4$ (0% SOC).

Even better marker of charged state is $F_{2g}(1)$ peak. $F_{2g}(1)$ scattering peak relates to lithium sublattice vibration and its intensity should decrease during a lithium deintercalation process [31]. Appearance of intense $F_{2g}(1)$ peak testifies highly lithiated phase [31]. We plotted intensity of this peak and found that it was absent in the middle of the particle, while it dominates at the border.

The particles from fresh and aged cathodes revealed a difference in the distribution of the extracted parameters (Figure 3e–h). The F_{2g}/A_{1g} peaks intensity ratio distribution for aged cathodes had statistical deviation significantly larger than in fresh cathodes. That means that lithiation is more inhomogeneous in the cathode. Not all regions of the particles play a role in lithiation/delithiation process in the cathode. The maximal real 'state of charge' for aged samples thereby decreases leading to general capacity fade of the battery. This result is consistent as well with the $F_{2g}(1)$ peak behavior. We could not analyze the distribution of the peak positions due to their low intensity and, consequently, high statistical error. Nevertheless, it is seen that normalized peak intensity is higher in fresh cathodes, which suggests stronger lithiation of the cathode. Freshly lithiated sample demonstrated small increase of peaks near 660 cm^{-1} connected to A_{1g} mode of Mn_3O_4, however high experimental noise makes spatial resolution more difficult in this phase.

3.3. Characterization of Delithiated State

At the next step, we analyzed delithiated samples. The principal difference of Raman spectra in lithiated and delithiated cathodes was noted. $Li_xMn_2O_4$ delithiation up to state with $x < 0.6$ involves the phase transition from *Fd3m* to *F43m* phase, leading to rearrangement of Raman modes. F_{2g} mode is substituted by the A_1 mode, while A_{1g} mode is substituted by F_2. At the same time, the position of the peaks remains almost the same: about 590 cm^{-1} and about 630 cm^{-1} (Figure 1b). Independently of the change of vibration modes the intensity of the peak at ~590 cm^{-1} gradually increases with delithiation, while peak at ~630 cm^{-1} gradually decreases [31].

We repeated the measurements of the maps using A_1 and F_2 band peak position (Figure 4). The peak position maps were essentially heterogeneous for both samples. The regions with large and small frequency shifts were mixed in the interior and edges of the particles. As discussed above, change of the lithiation state induces peak shift in the opposite direction. More lithiated phase corresponds to regions with F_2 band shift to lower frequency and A_1 band shift to higher frequency. However, some

regions do not show this behavior (Figure 4, selected area). We suggest that the formation of additional phase with scattering peaks at the similar frequencies is responsible for this effect. Besides, we observed the scattering peak at 660 cm^{-1} related to the A_{1g} vibration of Mn_3O_4 phase for delithiated particles, which increases in intensity at the particle interior. We did not observe intense scattering peak with similar frequency for lithiated cathodes.

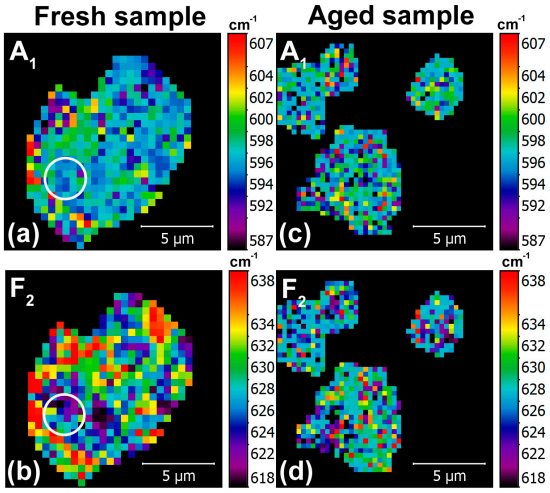

Figure 4. Mapping of the (**a**,**c**) A_1 and (**b**,**d**) F_2 peak positions in the active ionic particles of (**a**,**b**) fresh and (**c**,**d**) aged LMO cathodes. Delithiated state: $Li_{0.6}Mn_2O_4$ (100% SOC).

In order to resolve different phases of this heterogeneous system, we plotted separately the ratio between A_1 and F_2 intensities and demonstrated inhomogeneity of delithiation as well as intensity of A_{1g} band of Mn_3O_4 phase (Figure 5). The images confirmed formation of regions with dominant signal from Mn_3O_4 phase appearing as a result of battery intercalation/deintercalation, while in other regions in the particles ratio of A_1 and F_2 intensities revealed the distribution of lithiation state. More delithiatied regions were preferably localized at the particle borders oppositely to the case of lithiated state.

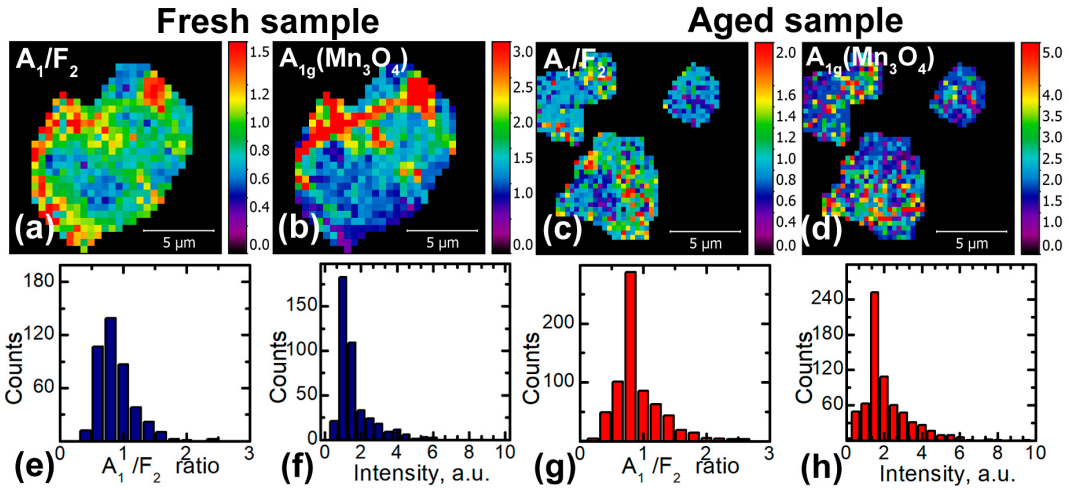

Figure 5. Mapping of the (**a**,**c**) ratio between A_1/F_2 peak intensities; (**b**,**d**) intensity of A_{1g} peak related to Mn_3O_4 phase in the active ionic particles of (**a**,**b**) fresh and (**c**,**d**) aged LMO cathodes; (**e**–**h**) histograms of the signal corresponding to maps (**a**–**d**). Delithiated state: $Li_{0.6}Mn_2O_4$ (100% SOC).

3.4. Cluster Analysis of the confocal Raman Spectroscopy Images

The cluster analysis is an approach based on the separation of the Raman spectra at the map to a few classes with the similar features. Here we used implementation of K-means clustering incorporated in Witec Project software [41]. This approach allowed to select areas with inhomogeneous variations of SOC and with M_3O_4 phase appeared as a result of $LiMn_2O_4 \rightarrow Mn_3O_4$ phase transformation. The cluster analysis was based on our findings presented in Sections 3.2 and 3.3. We obtained similar results on the distributions (but without any anomalies) by realizing clustering into three classes for fresh samples and two classes for aged samples (Figure 6).

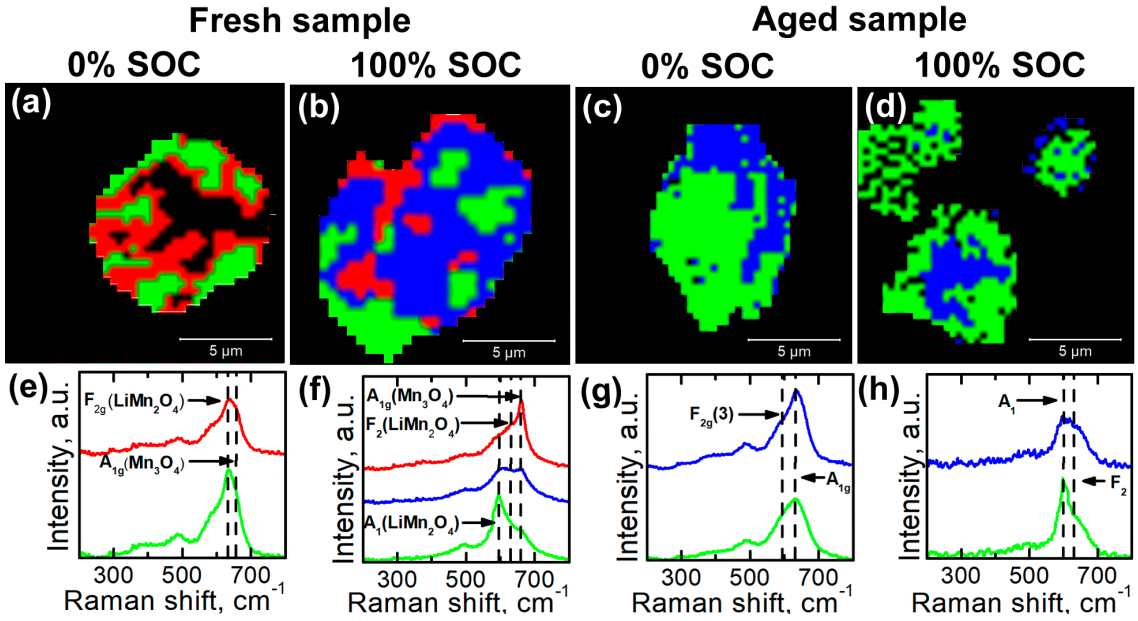

Figure 6. Cluster analysis of CRM images for LMO particles with different SOH and SOC. (**a**,**b**) lithiated and delithiated state for aged cathodes; (**c**,**d**) lithiated and delithiated state for fresh cathodes. Blue color: higher lithiated state, green color: less lithiated state, red color: Mn_3O_4; (**e**–**h**) Averaged Raman spectra from selected clusters with marked vibration modes corresponding to upper images. Dashed lines identify major lines in spectra related to 'state of charge' and Mn_3O_4 phase.

The particles revealed a distinct separation of the clusters with different 'state of charge'. Actually, the ion concentration profile has to be changed smoothly, but this approximation is valid in case of a sharp profile, appearing due to specific kinetics of lithiation accompanied with the formation of the lower lithiation state in the center of particle and higher lithiation state near the particle edge (so-called, 'radial model') [38,42]. Such a structure can be caused by slowing down the ionic mobility in the middle of the particle due to reduction of the local potential. In this experimental situation, concentration of the lithium ions increases too fast near the particle edge and, therefore, potential of the particles decreases and lithiation stops prematurely at lower lithiated cores of particles.

Freshly lithiated sample did not demonstrate any inhomogeneity of the state of charge. However, near the particle edge, we could clearly indentify the cluster in the subsurface region attributed to Mn_3O_4 phase (peak at ~660 cm^{-1}). Delithiated fresh particles also revealed regions with Mn_3O_4 phase. It is interesting to note also that the position of Mn_3O_4 often correlates with the cracks on the particles surface revealed by optics, which means that appearance of Mn_3O_4 phase can be responsible for the appearance of the stress in the material. On the contrary, Mn_3O_4 phase was not revealed in aged cathodes, which probably evidences that the dissolution of this phase occurs mostly at the beginning of cycling while further mechanism of capacitance fade is due to inhomogeneity of the delithiation process.

4. Conclusions

We used confocal Raman spectroscopy approach for studying intercalation/deintercalation processes in lithium manganese spinel cathodes. Precise analysis of the Raman spectra acquired on large areas of active particles combined with spatially resolved ones (inside the individual particles) could shed light on the main features of inhomogeneous lithiation and delithiation kinetics. Major parameters of the local Raman spectra reflecting 'state of charge' of active particles thus allowing visualization of its local distribution were found. The lithiation pathway was found to occur via the formation of the spatially inhomogeneous Li distribution in the middle of the particles and their edges. It was shown that cycling leads to: (1) formation of Mn_3O_4 phase with its further dissolution in the electrolyte; (2) qualitative change in the lithiation process in cycled LMO cathodes with significant inhomogeneity of the formed lithiation state. These processes are believed to be responsible for the capacity fade in the real battery cathodes. We demonstrated how the cluster analysis could be used in the confocal Raman microscopy imaging of electrode materials for the separation of various structural phases and lithiation states. In contrast to X-ray tomography and scanning transmission electron microscopy, confocal Raman microscopy does not require special sample preparation and, therefore, can be easily performed on commercial batteries. The implementation of the proposed approach, supplemented by advanced statistical analysis methods, opens up new perspectives in the understanding of intercalation/deintercalation kinetics in electrode materials.

Author Contributions: Denis Alikin and Boris Slautin conceived and designed the experiments; Daniele Rosato and Denis Alikin prepared samples for measurements; Boris Slautin performed the experiments; Denis Alikin and Boris Slautin analyzed the data; Dmitry Pelegov and Vladimir Shur reviewed the paper; Denis Alikin, Boris Slautin and Andrei Kholkin wrote the paper.

Acknowledgments: This research was made possible by the Russian Science Foundation (Grant 17-72-10144). The equipment of the Ural Center for Shared Use "Modern nanotechnology" UrFU was used.

Conflicts of Interest: The authors declare no conflict of interest. The founding sponsors had no role in the design of the study; in the collection, analyses, or interpretation of data; in the writing of the manuscript, and in the decision to publish the results.

References

1. Thackeray, M.M.; Johnson, P.J.; De Picciotto, L.A.; Bruce, P.G.; Goodenough, J.B. Electrochemical Extraction of Lithium from $LiMn_2O_4$. *Mater. Res. Bull.* **1984**, *19*, 179–187. [CrossRef]
2. Ohzuku, T.; Kitagawa, M.; Hirai, T. Electrochemistry of Manganese Dioxide in Lithium Nonaqueous Cell. *J. Electrochem. Soc.* **1990**, *137*, 769–775. [CrossRef]
3. Thackeray, M.M.; David, W.I.F.; Bruce, P.G.; Goodenough, J.B. Lithium Insertion into Manganese Spinels. *Mater. Res. Bull.* **1983**, *18*, 461–472. [CrossRef]
4. Fridman, K.; Sharabi, R.; Elazari, R.; Gershinsky, G.; Markevich, E.; Salitra, G.; Aurbach, D.; Garsuch, A.; Lampert, J. A New Advanced Lithium Ion Battery: Combination of High Performance Amorphous Columnar Silicon Thin Film Anode, 5V $LiNi_{0.5}Mn_{1.5}O_4$ Spinel Cathode and Fluoroethylene Carbonate-Based Electrolyte Solution. *Electrochem. Commun.* **2013**, *33*, 31–34. [CrossRef]
5. Julien, C.M.; Massot, M. Lattice Vibrations of Materials for Lithium Rechargeable Batteries I. Lithium Manganese Oxide Spinel. *Mater. Sci. Eng. B* **2003**, *97*, 217–230. [CrossRef]
6. Baddour-Hadjean, R.; Pereira-Ramos, J.-P. Raman Microspectrometry Applied to the Study of Electrode Materials for Lithium Batteries. *Chem. Rev.* **2010**, *110*, 1278–1319. [CrossRef] [PubMed]
7. Tang, D.; Sun, Y.; Yang, Z.; Ben, L.; Gu, L.; Huang, X. Surface Structure Evolution of $LiMn_2O_4$ Cathode Material upon Charge/discharge. *Chem. Mater.* **2014**, *26*, 3535–3543. [CrossRef]
8. Xia, Y.; Zhou, Y.; Yoshiot, M. Capacily Fading on Cycling of 4V Li/$LiMn_2O_4$. *Cells* **1997**, *144*, 4–11. [CrossRef]
9. Gummow, R.J.; de Kock, A.; Thackeray, M.M. Improved Capacity Retention in Rechargeable 4V Lithium/Lithium-Manganese Oxide (Spinel) Cells. *Solid State Ionics* **1994**, *69*, 59–67. [CrossRef]
10. Julien, C.; Mauger, A.; Vijh, A.; Zaghib, K. *Lithium Batteries. Science and Technology*; Springer International Publishing: Cham, Switzerland, 2007; pp. 175–184. ISBN 978–3-319-19108-9.

11. Du Pasquier, A. Mechanism for Limited 55 °C Storage Performance of $Li_{1.05}Mn_{1.95}O_4$ Electrodes. *J. Electrochem. Soc.* **1999**, *146*, 428. [CrossRef]
12. Zhan, C.; Wu, T.; Lu, J.; Amine, K. Dissolution, Migration, and Deposition of Transition Metal Ions in Li-Ion Batteries Exampled by Mn-Based Cathodes—A Critical Review. *Energy Environ. Sci.* **2018**, *11*, 243–257. [CrossRef]
13. Ebner, M.; Marone, F.; Stampanoni, M.; Wood, V. Visualization and Quantification of Electrochemical and Mechanical Degradation in Li Ion Batteries. *Science* **2013**, *342*, 716–721. [CrossRef] [PubMed]
14. Alikin, D.O.; Romanyuk, K.N.; Slautin, B.N.; Rosato, D.; Shur, V.Y.; Kholkin, A.L. Quantitative Characterization of the Ionic Mobility and Concentration in Li-Battery Cathodes via Low Frequency Electrochemical Strain Microscopy. *Nanoscale* **2018**, *10*, 2503–2511. [CrossRef] [PubMed]
15. Sun, Y.K.; Hong, K.J.; Prakash, J. The Effect of ZnO Coating on Electrochemical Cycling Behavior of Spinel $LiMn_2O_4$ Cathode Materials at Elevated Temperature. *J. Electrochem. Soc.* **2003**, *150*, A970. [CrossRef]
16. Thackeray, M.M.; Johnson, C.S.; Kim, J.S.; Lauzze, K.C.; Vaughey, J.T.; Dietz, N.; Abraham, D.; Hackney, S.A.; Zeltner, W.; Anderson, M.A. ZrO_2- and Li_2ZrO_3-Stabilized Spinel and Layered Electrodes for Lithium Batteries. *Electrochem. Commun.* **2003**, *5*, 752–758. [CrossRef]
17. Ram, P.; Gören, A.; Ferdov, S.; Silva, M.M.; Singhal, R.; Costa, C.M.; Sharma, R.K.; Lanceros-Méndez, S. Improved Performance of Rare Earth Doped $LiMn_2O_4$ Cathodes for Lithium-Ion Battery Applications. *New J. Chem.* **2016**, *40*, 6244–6252. [CrossRef]
18. Liu, Q.; Wang, S.; Tan, H.; Yang, Z.; Zeng, J. Preparation and Doping Mode of Doped $LiMn_2O_4$ for Li-Ion Batteries. *Energies* **2013**, *6*, 1718–1730. [CrossRef]
19. Leger, C.; Bach, S.; Soudan, P.; Pereira-Ramos, J.P. Structural and Electrochemical Properties of ω $Li_xV_2O_5$ ($0.4 \leq X \leq 3$) as Rechargeable Cathodic Material for Lithium Batteries. *J. Electrochem. Soc.* **2005**, *152*, A236–A241. [CrossRef]
20. Itoh, T.; Sato, H.; Nishina, T.; Matue, T.; Uchida, I. In Situ Raman Spectroscopic Study of Li_xCoO_2 Electrodes in Propylene Carbonate Solvent Systems. *J. Power Sources* **1997**, *68*, 333–337. [CrossRef]
21. Inaba, M.; Iriyama, Y.; Ogumi, Z.; Todzuka, Y.; Tasaka, A. Raman Study of Layered Rock-Salt $LiCoO_2$ and Its Electrochemical Lithium Deintercalation. *J. Raman Spectrosc.* **1997**, *28*, 613–617. [CrossRef]
22. Dokko, K.; Mohamedi, M.; Anzue, N.; Itoh, T.; Uchida, I. In Situ Raman Spectroscopic Studies of $LiNi_xMn_{2-x}O_4$ Thin Film Cathode Materials for Lithium Ion Secondary Batteries. *J. Mater. Chem.* **2002**, *12*, 3688–3693. [CrossRef]
23. Harris, S.J.; Rahani, E.K.; Shenoy, V.B. Direct In Situ Observation and Numerical Simulations of Non-Shrinking-Core Behavior in an MCMB Graphite Composite Electrode. *J. Electrochem. Soc.* **2012**, *159*, A1501–A1507. [CrossRef]
24. Harris, S.J.; Timmons, A.; Baker, D.R.; Monroe, C. Direct in Situ Measurements of Li Transport in Li-Ion Battery Negative Electrodes. *Chem. Phys. Lett.* **2010**, *485*, 265–274. [CrossRef]
25. Migge, S.; Sandmann, G.; Rahner, D.; Dietz, H.; Plieth, W. Studying Lithium Intercalation into Graphite Particles via in Situ Raman Spectroscopy and Confocal Microscopy. *J. Solid State Electrochem.* **2005**, *9*, 132–137. [CrossRef]
26. Kostecki, R.; McLarnon, F. Local-Probe Studies of Degradation of Composite $LiNi_{0.8}Co_{0.15}Al_{0.05}O_2$ Cathodes in High-Power Lithium-Ion Cells. *Electrochem. Solid-State Lett.* **2004**, *7*, A380. [CrossRef]
27. Kerlau, M.; Marcinek, M.; Srinivasan, V.; Kostecki, R.M. Reprint of "Studies of Local Degradation Phenomena in Composite Cathodes for Lithium-Ion Batteries. " *Electrochim. Acta* **2007**, *53*, 1386–1393. [CrossRef]
28. Nishi, T.; Nakai, H.; Kita, A. Visualization of the State-of-Charge Distribution in a $LiCoO_2$ Cathode by In Situ Raman Imaging. *J. Electrochem. Soc.* **2013**, *160*, A1785–A1788. [CrossRef]
29. Nanda, J.; Remillard, J.; O'Neill, A.; Bernardi, D.; Ro, T.; Nietering, K.E.; Go, J.Y.; Miller, T.J. Local State-of-Charge Mapping of Lithium-Ion Battery Electrodes. *Adv. Funct. Mater.* **2011**, *21*, 3282–3290. [CrossRef]
30. Pelegov, D.V.; Slautin, B.N.; Gorshkov, V.S.; Zelenovskiy, P.S.; Kiselev, E.A.; Kholkin, A.L.; Shur, V.Y. Raman Spectroscopy, "Big Data", and Local Heterogeneity of Solid State Synthesized Lithium Titanate. *J. Power Sources* **2017**, *346*, 143–150. [CrossRef]
31. Ammundsen, B.; Burns, G.R.; Islam, M.S.; Kanoh, H.; Roziere, J. Lattice Dynamics and Vibrational Spectra of Lithium Manganese Oxides: A Computer Simulation and Spectroscopic Study. *J. Phys. Chem. B* **1999**, *103*, 5175–5180. [CrossRef]

32. Sinha, M.M.; Gupta, H.C. Study of Zone-Center Phonons in Lithium Manganese Oxide. *Phys. B Condens. Matter* **2002**, *316*, 166–169. [CrossRef]
33. Anzue, N. In Situ Raman Spectroscopic Study of Thin-Film $Li_{1-x}Mn_2O_4$ Electrodes. *Solid State Ionics* **2003**, *156*, 301–307. [CrossRef]
34. Kanoh, H.; Tang, W.; Ooi, K. In Situ Raman Spectroscopic Study on Electroinsertion of Li+ into a Pt/λ-MnO_2 Electrode in Aqueous Solution. *Electrochem. Solid-State Lett.* **1998**, *1*, 17–19. [CrossRef]
35. Ramana, C.V.; Massot, M.; Julien, C.M. XPS and Raman Spectroscopic Characterization of $LiMn_2O_4$ Spinels. *Surf. Interface Anal.* **2005**, *37*, 412–416. [CrossRef]
36. Gao, Y.; Reimers, J.N.; Dahn, J.R. Changes in the Voltage pro Le of $Li/Li_{1-x}Mn_{2-x}O_4$ Cells as a Function of X. *Phys. Rev. B* **1996**, *54*, 3878–3883. [CrossRef]
37. Nishizawa, M.; Ise, T.; Koshika, H.; Itoh, T.; Uchida, I. Electrochemical In-Situ Conductivity Measurements for Thin Film of $Li_{1-x}Mn_2O_4$ Spinel. *Chem. Mater.* **2000**, *12*, 1367–1371. [CrossRef]
38. Luchkin, S.Y.; Amanieu, H.Y.; Rosato, D.; Kholkin, A.L. Li Distribution in Graphite Anodes: A Kelvin Probe Force Microscopy Approach. *J. Power Sources* **2014**, *268*, 887–894. [CrossRef]
39. Alikin, D.O.; Ievlev, A.V.; Luchkin, S.Y.; Turygin, A.P.; Shur, V.Y.; Kalinin, S.V.; Kholkin, A.L. Characterization of $LiMn_2O_4$ Cathodes by Electrochemical Strain Microscopy. *Appl. Phys. Lett.* **2016**, *108*, 113106. [CrossRef]
40. Amanieu, H.Y.; Aramfard, M.; Rosato, D.; Batista, L.; Rabe, U.; Lupascu, D.C. Mechanical Properties of commercial $Li_xMn_2O_4$ cathode under Different States of Charge. *Acta Mater.* **2015**, *89*, 153–162. [CrossRef]
41. Dieing, T.; Hollricher, O.; Toporski, J. *Confocal Raman Microscopy*; Springer-Verlag: Berlin, Germany, 2010; pp. 75–83. ISBN 978-3-642-12521-8.
42. Andersson, A.S.; Thomas, J.O. The Source of First-Cycle Capacity Loss in $LiFePO_4$. *J. Power Sources* **2001**, *97*, 498–502. [CrossRef]